Design and Test of an Improved Active Disturbance Rejection Control System for Water Sampling Unmanned Surface Vehicle

Defeng Wu[a,b,*], Kexin Yuan[a], Youqiang Huang[a], Zhi-Ming Yuan[c] and Lisha Hua[d]

[a]School of Marine Engineering, Jimei University, Xiamen 361021, PRC
[b]Fujian Provincial Key Laboratory of Naval Architecture and Ocean Engineering, Xiamen 361021, PRC
[c]Department of Naval Architecture, Ocean & Marine Engineering, University of Strathclyde, Glasgow, G4 0LZ, United Kingdom.
[d]College of Engineering, City University of Hong Kong, PRC

ARTICLE INFO

Keywords:
water sampling unmanned surface vehicle
active disturbance rejection control
extreme learning machine
input constraints
human machine interaction

ABSTRACT

Unmanned surface vehicles (USVs) have wide application prospects in military and civil fields. Motivated by the large demand for environmental protection equipment, a water-sampling USV (WS-USV) system is designed in this study. The software and hardware of the entire system are designed and developed independently. Two water sampling modes, a manual remote control mode and remote interface automatic control mode are designed for handling emergencies. The WS-USV is propelled by twin-propellers. These propellers have many input constraints owing to their inherent structure, making the design of the controller very difficult. In this study, an improved active disturbance rejection control (ADRC) method is proposed and a saturation function is introduced to design a path-following control system for the WS-USV. This enhances the anti-disturbance ability for addressing environmental disturbances by wind, waves and currents in the water sampling process. The stability of the system is improved. The feasibility, stability and performance superiority of the control system are proven by water sampling contrast experiments.

1. Introduction

Approximately 70% of the earth's surface is covered by water. With the rapid development of industrialisation, the pollution of rivers, lakes, and other water resources is becoming increasingly serious [1]. Despite being a source of life, fresh water is scarce in most countries, and extremely lacking in others. To this end, all countries have actively taken necessary measures to protect rivers and lakes, so that the overall quality of the ecological water environment is improved. The efficient acquisition of water samples is not only a prerequisite for the prevention and control of water pollution, but is also the premise for improving the water environment, restoring the functions of rivers and lakes, and ensuring the safety of the water. At present, environmental monitoring authorities mainly conduct manual sampling and online sampling. Manual sampling has the disadvantages of a long collection cycle, high work intensity, low efficiency and even great potential safety hazards to human health. Online sampling is limited to collecting water samples from fixed points, and cannot be widely used in large water areas, owing to high cost and without random dynamics [2].

Owing to developments in automatic control theory and related technologies, autonomous underwater vehicles (AUVs), unmanned surface vehicles (USVs), ground robots, and unmanned aerial vehicles (UAVs) are rapidly emerging [3]. The sea, land, and air vehicles gradually tend to be integrated and unmanned [4], which has aroused the enthusiasm of scholars and researchers. Among them, USVs have been widely used in military and civilian fields [5, 6]. Different functions can be achieved by installing different modules on USVs. A water sampling USV (WS-USV) was developed by carrying a water sampling module on a USV. Research on the control system of the WS-USV has great significance for improving the ecological environment, reducing the sampling cost, and increasing the safety of sampling personnel.

Existing research on USVs can be divided into two categories: theoretical studies of control strategies, and control system designs for the USV. In terms of theoretical research, many control methods have been used in USVs, including proportional-integral-derivative (PID) control [7, 8, 9], sliding mode control (SMC) [10, 11, 12], fuzzy control [13, 14, 15], active disturbance rejection control (ADRC) [16] and dynamic surface control (DSC) [17]. However, the above methods have limited abilities to defend against environmental forces and model uncertainties. In ref.[18], an adaptive dynamic surface trajectory tracking control method was proposed based on a neural network (NN). The model uncertainties were estimated using a radial basis function NN (RBF-NN), and the input saturation of the rudder was compensated for by an auxiliary design system. Park et al.[19] proposed a NN-based output feedback control method, and the speed of the USV was estimated by an NN observer. A path-following control method of USVs based on backstepping technology and principle of line-of-sight (LOS) navigation was proposed by Peng et al.[20]. The USV suffered from complex disturbances and speed and output constraints, which were compensated for and adjusted by an extended state observer (ESO) and reference regulator, respectively. An adaptive NN-based trajectory fault-tolerant tracking control method for a USV was proposed in ref.[21]. The NN technology was used to address model uncertainties. The adaptive method and a backstepping technique were combined to handle input saturations, disturbances, and actua-

*corresponding author.
arcwdf@gmail.com (Defeng Wu)
ORCID(s):

tor faults. A novel data-driven backstepping path-following control strategy was proposed by Weng et al.[22], in which the backstepping technology and sliding mode surface were combined to simplify the design of the controller and enhance robustness. The ESO was used to compensate for complex unknowns. In ref.[23], a fixed-time conversion control method was proposed. The dynamic model of the USV was transformed into two cascading subsystems to address actuator dead zones. A finite-time nonlinear SMC method was proposed in ref.[24]. A terminal sliding mode controller and auxiliary sliding mode controller were used to control different state areas to avoid singular problems. An adaptive NN position tracking control method was proposed by Zhang et al.[25]. The backstepping technology, NN, DSC, and SMC methods were combined to design a robust controller, in which the estimation of model parameters was avoided, and the potential for practical application was improved. A reinforcement learning (RL) controller was proposed in ref.[26], an NN-based RL method was introduced to compensate for uncertainties and disturbances. The advanced control methods mentioned above all showed superior control effects, but applying them to actual control systems requires further study and simplification.

The design of a control system is relatively slow, and there are few scholars studying this area. The ones that do mainly focus on traditional control methods [27, 28, 29, 30, 31]. For example, a LOS-based PID control strategy was proposed for an under-actuated vehicle by Caharija et al.[27]. A P-speed controller with linear feedback and PD-heading controller with linear feedback were designed for the control of an under-actuated AUV, and sea tests were conducted to verify the effectiveness and stability of the proposed control strategy and designed controller. A NN-based output feedback control method was proposed for a twin-propeller USV with input saturation by Chenet al.[28]; they designed a trajectory tracking controller for the USV. The effectiveness of the controller was verified through simulations and experiments. In ref.[29], a fuzzy PID-based trajectory tracking control system was designed for a river crab feeding boat with twin paddle wheels, and the effectiveness and reliability of the control system were validated by feeding experiments. An LOS navigation-based target enclosing strategy for USVs was proposed by Jiang et al.[30], and its feasibility was verified through simulation experiments. A control system based on the ADRC method was also designed. The effectiveness of the control strategy and stability of the control system were verified by a target enclosing experiment with two triple-propeller single-rudder USVs. A novel translation and rotation cascade control method was proposed in ref.[31]. First, the superiority of this method was verified by comparative simulation experiments. Then, a path-following controller for a twin-propeller USV was designed using this method. The feasibility of the control strategy and effectiveness of the controller were verified through experiments. A UAV sampling remote control system for mine water samples was developed by Banerjee et al.[32]. It could sample in small, isolated, and dangerous water areas, and could avoid the dangers in traditional sampling methods. In ref.[33], a water sampling UAV was developed by designing a water sampling device and equipping it on a UAV, which improved the sampling efficiency and safety. As can be seen from the above references, there is little research and design regarding the unmanned sampling equipment urgently needed for environmental monitoring, especially in regards to the design of WS-USV systems. Motivated by the urgent demand for environmental protection equipment, and drawing on experience from improving the anti-disturbance effects of controllers used in RL, NN or other learning (optimization) methods to approximate an unknown state in theoretical research[34], an improved ADRC strategy combining traditional ADRC with extreme learning machine (ELM) is proposed in this study. The strategy considers the practical problems of the propeller (with various input and output constraints) and system stability, and a set of control systems for the WS-USV is designed by introducing a saturation function and combining it with the improved ADRC method. The control system is applied to a WS-USV for independent design and development. The effectiveness, stability, and superiority of the control method and control system are verified by water sampling contrast experiments. The main contributions of this study are as follows:

(1). A set of WS-USV systems is independently designed. To facilitate emergency treatment, a manual remote control device and remote automatic control platform are designed for the WS-USV.

(2). An improved ADRC strategy is proposed, and a WS-USV path-following control system is designed based on this control strategy.

(3). Considering that the stability of the system will be greatly affected by the propeller working under extreme conditions for a long time, a saturation function is introduced in the design of the control system, to solve the multiple input constraints of the WS-USV system caused by the inherent structure of the propellers. Based on ensuring a good control effect, this function not only reduces wear, but also enhances the stability of the system.

The organisation of this paper is as follows. The hardware and software architecture is introduced in Section II. In Section III, the control strategy of the WS-USV is introduced, and the improved active disturbance rejection controller is designed. Section IV provides the water sampling experimental results. The conclusion is presented in Section V.

2. Framework of water-sampling unmanned surface vehicle (WS-USV) system

2.1. Overall design of WS-USV system

The overall structure of the WS-USV is shown in Fig.1. The WS-USV system consists of an onboard subsystem and onshore subsystem. The onboard subsystem includes a GPS module, electronic compass module, rotatable camera module, ultrasonic distance measurement module, wireless communication module, ARM control module, twin-propeller

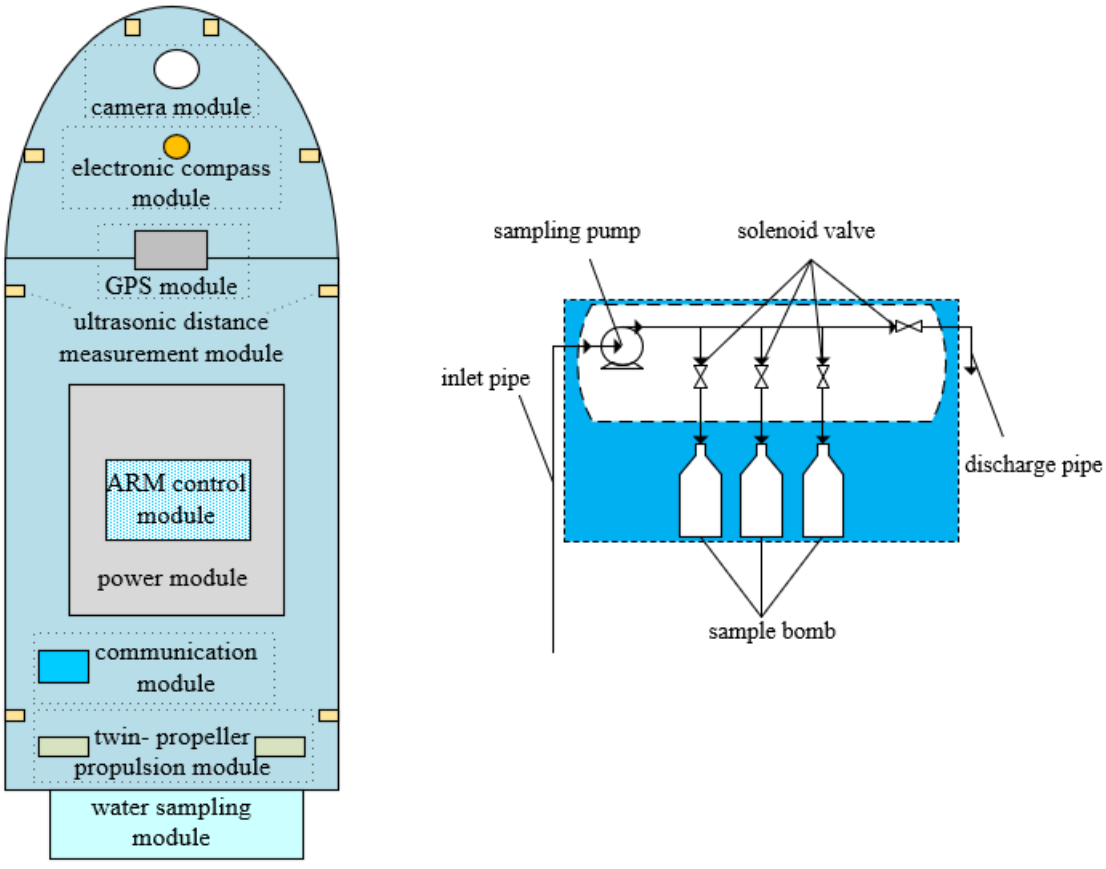

Figure 1: Structure diagram of water-sampling unmanned surface vehicle (WS-USV).

propulsion module, power module, 4G network image transmission module and water sampling module. The water sampling module is shown in Fig.1b. The onshore subsystem consists of a wireless communication module, joystick remote control module, and remote control platform. The hull of the WS-USV is constructed with fibre-reinforced plastic, propelled by the twin-propeller sat the stern of the WS-USV and steered by the rotation speed difference of the twin-propeller. A rotatable camera module is mounted on the bow, an ultrasonic distance measurement module is evenly distributed at port and starboard, the water sampling module is installed on the stern.

2.2. Hardware structure of the onboard subsystem

To meet the needs of various working environments and emergency situations, two control modes are designed for the WS-USV: a manual remote control sampling mode and automatic sampling mode. To reduce the risk of hardware failures caused by the switching of the two modes, the manual remote control part is developed in the remote automatic control platform. The hardware of the onboard system is centred on the ARM control module, which is the 'STM32F-429IGT6' designed and produced by STMicroelectronics. The microcontroller core is the Cortex-M4 designed by ARM, and the peripherals, such as the general purpose input output (GPIO), universal synchronous/asynchronous receiver/transmitter (USART), inter-integrated circuit (IIC) and serial peripheral interface are designed and produced by ST Microelectronics. Lithium battery power modules provide power for the entire onboard system. The RS232 serial interface and direct memory access (DMA) transmission mode are used, in which the ARM control module communicates with the GPS module, electronic compass module and wireless communication module. The IIC communication mode is adopted for when the ultrasonic distance measurement module communicates with the ARM control module. The ARM control module collects and centrally manages the data of the above modules, and combines it with the work task of the water sampling to produce corresponding two pulse width modulation (PWM) signals to drive the twin-propeller propulsion module to control the motion of the WS-USV. According to the sampling instructions, the water sampling module is controlled to collect water samples. The onboard wireless communication module is used for communication between the onboard and onshore subsystems. The rotatable camera module and 4G-network image transmission module are equipped for long-distance observation of the environment around the WS-USV and image target detection via image transmission. The data of the ultrasonic distance measurement module and image information are used to research collision avoidance. The hardware connections and communication modes of the WS-USV system are shown in Fig.2.

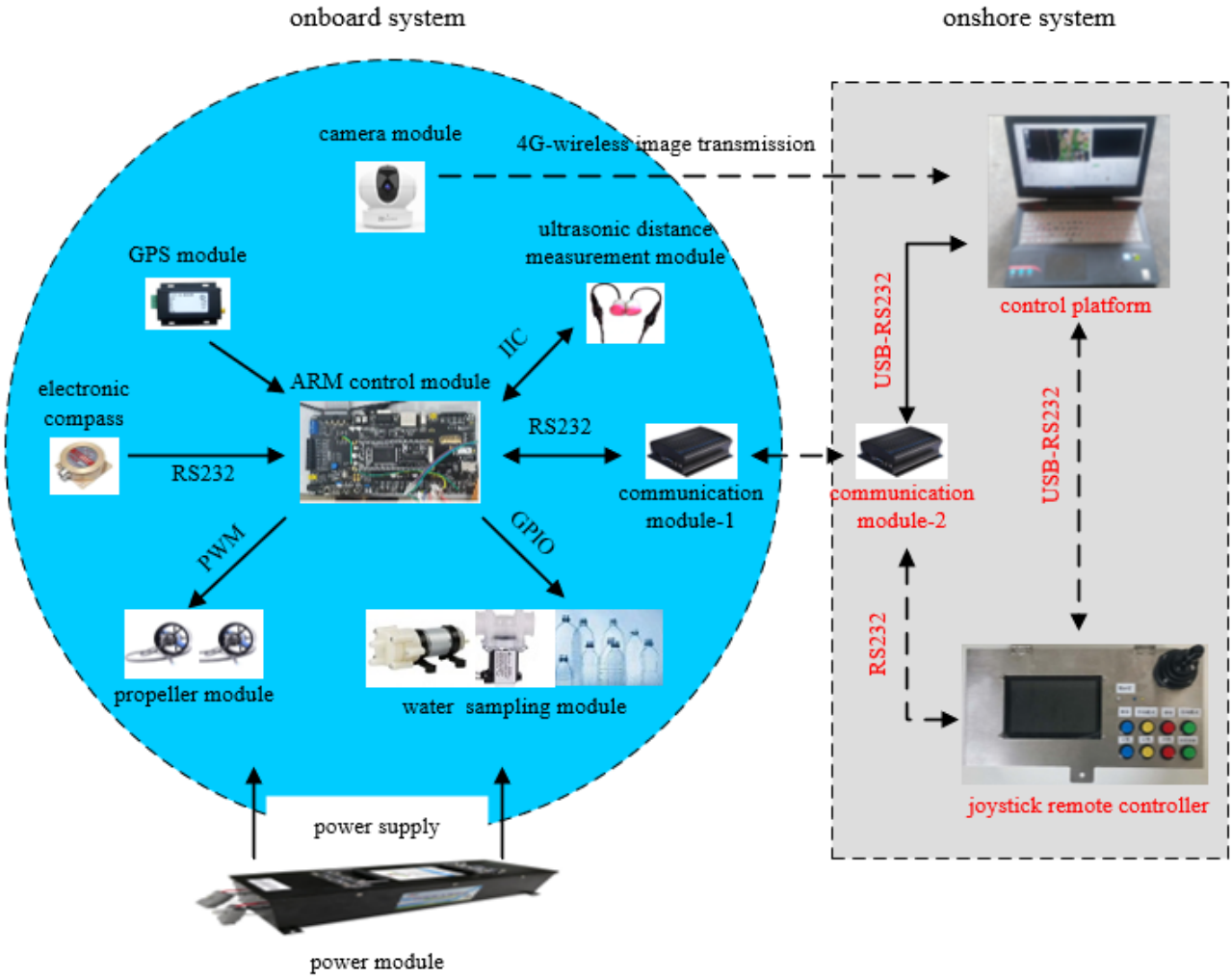

Figure 2: Hardware connections and communication modes of the WS-USV system.

2.3. Software development of the WS-USV system

2.3.1. Software design of the onboard subsystem

To ensure the portability of the system and openness of the interface, an embedded real-time uC/OS-III operating system is adopted in the onboard subsystem. The software design employs the concept that the data obtaining, processing, and sending of a module is designed as a subprogram. The software design of the onboard system is divided into two parts, the underlying bus and the configuration of peripherals (including the configuration of the drivers for the USART, IIC, DMA, GPIO, and PWM) [35]. The driver program is not only the link between the various hardware modules, but also acts as the bridge of the entire system. The driver program and corresponding control program perform data exchanges with each module, so that the onboard system can operate normally. The software structure of the onboard subsystem consists of a data acquisition module, processing module, output module, and communication module for interacting with the onshore subsystem. The acquisition module receives and incorporates GPS data, electronic compass data, ultrasonic probe data and communication module data. The processing module decodes the GPS, electronic compass, ultrasonic probe, and communication module data, and provides joint processing thereof. The output module incorporates the outputs of the PWM, on-off instructions of the relays, and transmissions of the communication module data. The overall software workflow of the onboard system is shown in Fig.3.

2.3.2. Software development of joystick remote controller

The program of the joystick remote controller also follows the concept that the data obtaining, processing, and sending of a module is designed as a subprogram. The overall control program is divided into main programs and some subprograms; the subprograms are comprised of the driver programs of each module. Each verified subprogram can be embedded in the main program.

After the joystick remote controller is initialised, the data of the joystick is received through the RS232 and DMA. To avoid jitter in the WS-USV data from shaking, the data is received multiple times, the shaking data is removed by the

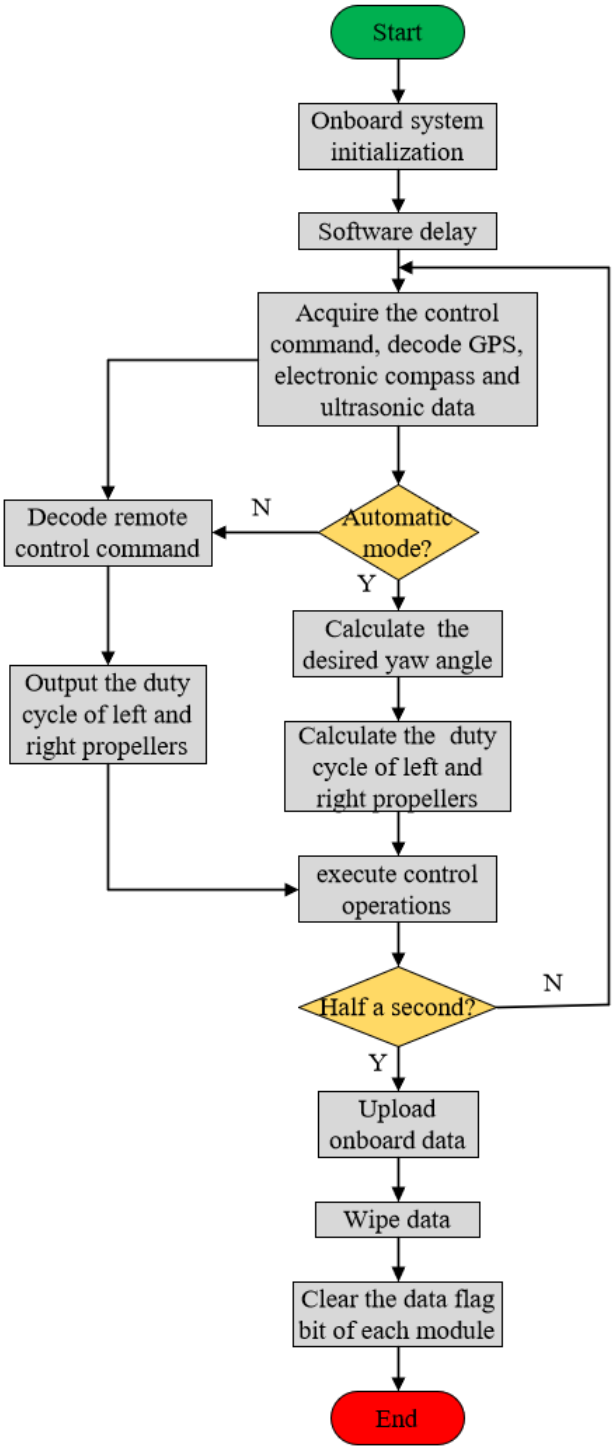

Figure 3: Workflow chart of the onboard subsystem.

median value filtering method. The filtered data is converted into corresponding control instructions. Then, by detecting whether a flag is set, it is determined whether effective data has been returned (received) from the WS-USV. If the flag is set, the data will be decoded according to the return protocol, and important data will be displayed on an LCD screen. Finally, there is confirmation of whether the status of each key has changed, and according to the key state changes, the corresponding control instructions are sent to the WS-USV to perform the corresponding operations. The overall workflow of the joystick remote controller is shown in Fig.4.

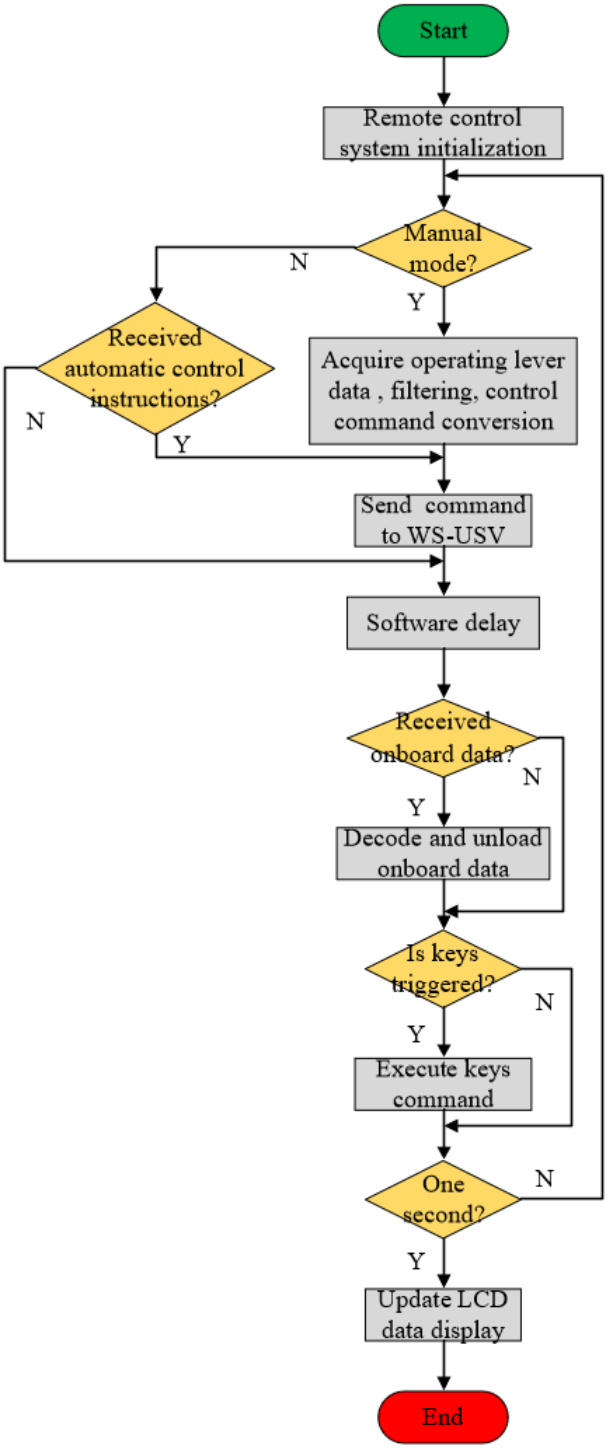

Figure 4: Workflow chart of the remote control subsystem

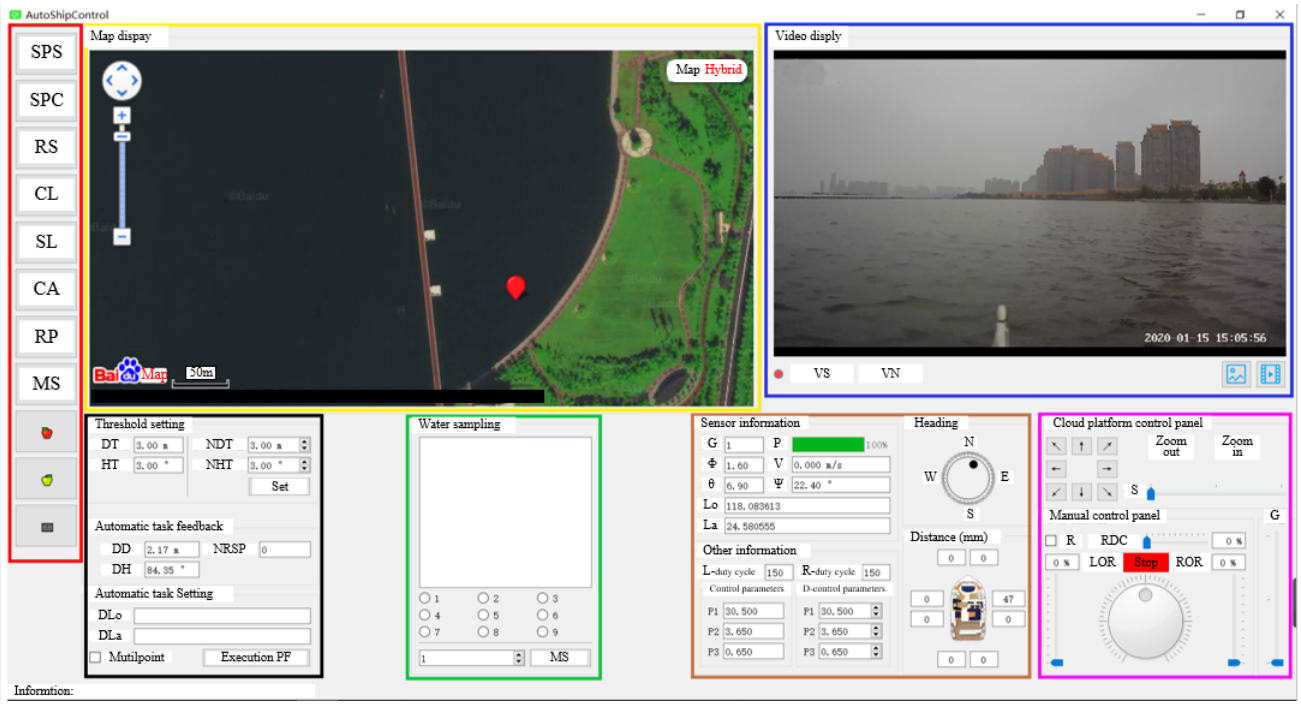

Figure 5: Human-machine interaction (HMI) of the remote control platform.

2.3.3. Design and development of the remote control platform

The control interface application of the remote automatic control platform is developed by QT application [36]. The human-machine interaction (HMI) of the WS-USV system is shown in Fig.5. It is divided into seven parts: auxiliary function selection zone, map display zone, automatic control operation zone, water sampling zone, video display zone, sensor parameter zone, and manual control zone.

Auxiliary function selection zone (red zone): This zone includes buttons for serial port setting, serial port connecting, reset sensor, clear log, storage log, chart analysis, refresh path, and mode switching. This zone is the auxiliary control function zone of the HMIs for the WS-USV. The communication between the control software and WS-USV is connected by the serial port setting button and connecting serial port button. The operation log of the WS-USV is managed using the clearing log and storage log buttons. The running real-time status information curve of the WS-USV is displayed through the chart analysis button. The sampling path of the WS-USV is updated through the refresh path button. The control mode of the WS-USV is switched by the mode switching button (i.e. to automatic control mode or manual control mode).

Map display zone (yellow zone): The application programming interface [37] of the Baidu Map is called to display the location and actual path of the WS-USV in real time. A point on the map can also be selected and marked as a water sampling point, which is then displayed on the map.

Automatic control operation zone (black zone): This zone includes three functions: threshold setting, automatic task feedback, and automatic task setting. The threshold setting function includes setting the distance and yaw angle thresholds. The automatic task feedback function includes displaying the desired distance, desired heading, and number of remaining sampling points. The automatic task setting function includes setting the longitude and latitude of the desired sampling points, and selecting single-point sampling or multi-point sampling.

Water sampling zone (green zone): This zone includes two functions: automatic water sampling and manual water sampling. The automatic water sampling function is based on the desired sampling points for automatic sampling; the sampling number and completed information are shown in the panel. The manual sampling function is an alternative function, e.g., when automatic sampling is not working, the operator can manually select the number of sampling points to complete the water sampling.

Video display zone (blue zone): This zone includes four functions: video acquisition parameter configuration, video connection, capture current video image, and video recording. The serial number, transmission address, channel number, key, screenshot, and/or video saving path of the camera module should be configured for video acquisition. The video connection function mainly concerns the connected video acquisition module, so that the video image is displayed on the control platform. The video images can be captured by the current video image function, and are saved to the specified path by number. The video returned by the camera module can be recorded in MP4 format the video recording video function, and is saved to the same path.

Parameter display zone (brown zone): This zone pro-

vides a dynamic display of the WS-USV status information, including the motion status information of the WS-USV, propulsion information, and distance information between the WS-USV and obstacles. The motion status information of the WS-USV includes the position, roll, pitch, yaw, speed, and battery level. The propulsion information includes the duty cycle values of the left and right propellers, control parameters of the controller, and adjustable desired control parameters.

Manual control zone (purple zone): This zone can be divided into two parts: cloud platform control and manual control. The rotation speed, recording angle, and recording range of the camera can be adjusted by the cloud platform control. The manual control of the WS-USV includes gear adjustment, propulsion direction setting, and course adjustment.

Remark 1. The overall operation process (single cycle) of the onboard subsystem programs and the remote control subsystem programs are illustrated in Fig.3 and Fig.4 respectively. The half-duplex communication mode is employed for the wireless data transmission station between the onboard and onshore subsystem. The workflow of manual remote control mode for the WS-USV system is described as follows: each subsystem is initialized firstly; the manual remote control mode is set by the operator later. After receiving the information from the joystick, the remote control subsystem transmits data to the onboard subsystem through communication module. After the onboard subsystem receives the data, the follow-up process is completed according to the respective process of two subsystems. Then the important onboard data is sent back to the onboard subsystem through communication module. After remote control subsystem receives relevant data and key commands, part of the important information received is displayed in the remote control subsystem. The single process is finished and the circulation cycles until the whole task is completed.

3. Autonomous motion control strategy for the WS-USV

During automatic water sampling, the operator first sends the desired sampling point information to the WS-USV using the remote control platform. After receiving the water sampling instruction, the desired yaw angle and desired distance between the actual position of the WS-USV and current target sampling point are calculated; for this calculation, the motion status information is collected by the onboard sensors. Then, the controller adjusts the heading of the WS-USV according to the desired yaw angle and current yaw angle, and sails to the desired sampling point at a certain speed. It begins sampling when the WS-USV reaches the target sampling area. After sampling, the WS-USV sails to the next sampling point in the same way. Based on this sampling strategy, the motion control principle diagram for the WS-USV, as designed in this study, is shown in Fig.6.

In Fig.6, ψ represents the current yaw angle of the WS-USV as collected by the electronic compass; ψ_d denotes the azimuth of the current position of the WS-USV and the desired position $\psi, \psi_d \in [0°, 360°]$, which are positive in the clockwise direction, when the heading point to north is 0°. d is the distance between the current position of the WS-USV and desired position, u_d is the set desired speed, and P_1 represents the reference duty ratio at the desired speed,and P_2 represents the output duty cycle of the controller. $P_c = [P_{c1}, P_{c2}]^T$ is the converted output value, and $P_1 = [P_{1l}, P_{1r}]^T$ is the vector consisting of the duty cycles corresponding to the desired speeds of the left and right propellers. $P = [P_{11}, P_{22}]^T$ denotes the vector comprising the control output after conversion and applying actual engineering restrictions.

The controller in the control schematic is designed for an improved ADRC strategy, in which the duty cycle for adjusting the heading of the WS-USV is calculated from the desired yaw angle and current yaw angle of the WS-USV (as acquired by the electronic compass module). Then, as combined with the reference duty cycle of the desired speed of the WS-USV, the rotation speeds of the left and right propellers are adjusted to control the motion of the WS-USV towards the desired course. The distance between the current position of the WS-USV and current desired sampling position is used to determine whether the WS-USV has reached the desired sampling point. Until the WS-USV reaches the desired sampling area, water sampling is performed automatically. To improve the sampling efficiency, motion in a straight line between sampling points is expected. A motion control strategy for the straight line is proposed based on the principle diagram for the WS-USV, and is divided into heading guidance and heading tracking control.

3.1. Heading guidance

In the process of moving the WS-USV from the current position to desired sampling position, the azimuth angle from the current position to target sampling point is taken as the desired yaw angle. The current yaw angle is acquired by the electronic compass. The yaw angle of the WS-USV is adjusted by the controller to change the rotation speed of the twin-propeller. Therefore, it can sail to the desired sampling point according to the expected heading. However, the WS-USV is disturbed by winds, waves, and currents. The guidance from the limited target points will cause the WS-USV to deviate from the desired path when tracking the desired course. To reduce control deviations, virtual target points [29] are introduced in the actual control process. Multiple virtual positions are calculated on the desired path between the current position of the WS-USV and target sampling position. The WS-USVfollowsthe multiple virtual positions, instead of directly tracking a single target sampling point. Therefore, the motion of the WS-USV can be corrected at a regular distance. Compared with directly tracking a target sampling point, this can indirectly reduce the distance for tracking the next target position, and any deviations between the actual path and desired path caused by disturbances. Thus, the performance of the followed path is improved by this method. A schematic of the virtual target

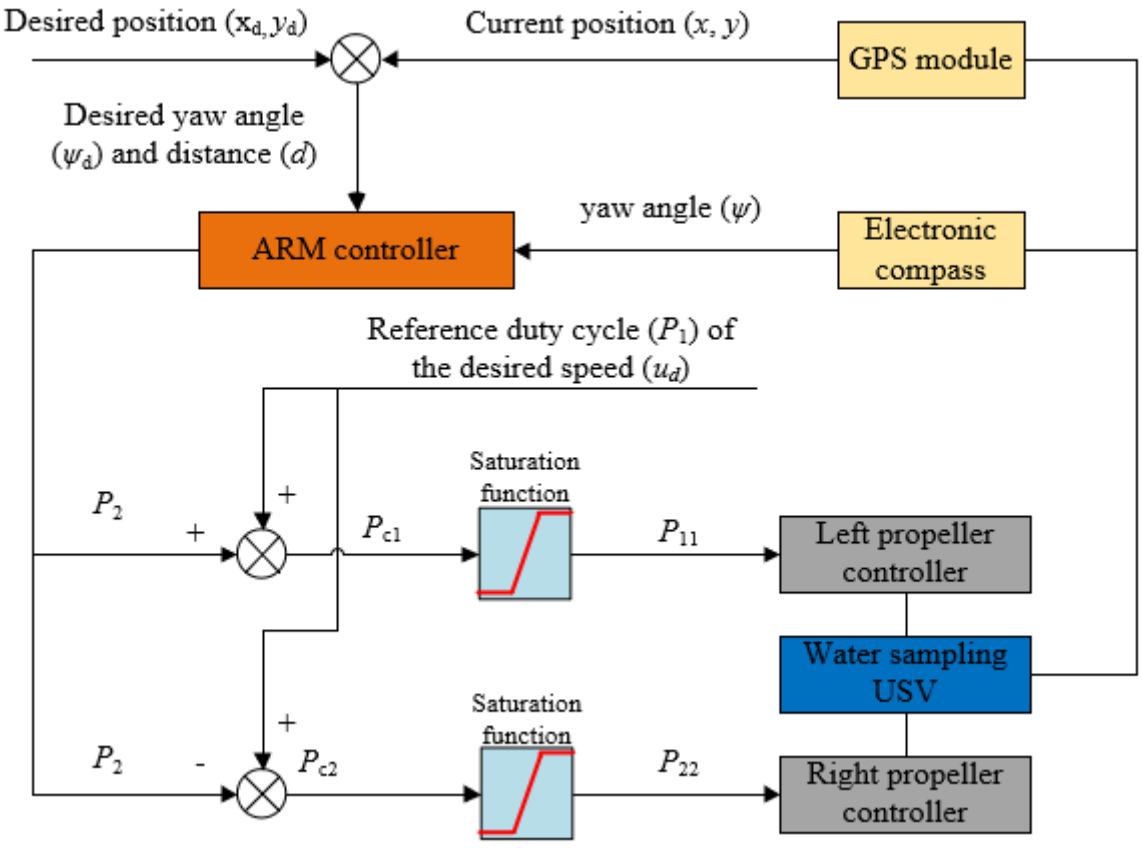

Figure 6: Control schematic of the WS-USV.

point calculation is shown in Fig.7.

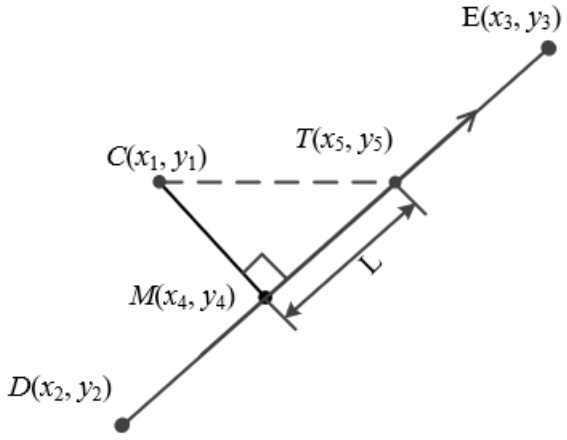

Figure 7: Schematic of the virtual position calculation [29].

In Fig.7, C represents the position of the WS-USV, D is the initial position, E is the desired position, T is the virtual position in the desired DE path, M is the projection point of the WS-USV position on the desired DE path, (x_i, y_i) is the longitude and latitude of each position $(i = 1, 2, 3, 4, 5)$; and L is the distance between the projection point of the WS-USV position and virtual target position on the desired DE path.

If the direction of line CE is taken as the guidance direction for the WS-USV, the WS-USV will have a larger deviation from the desired path of the line DE. However, if point T is taken as the first virtual target point, the direction of line CT is taken as the guiding direction until the WS-USV reaches the area of point T, and then continues to track the next virtual target point. Until the WS-USV reaches the area of the desired sampling point E, there is a superior path-following performance using this method. The longitude and latitude coordinates of point T are calculated as follows:

1. Calculate the longitude and latitude coordinates of the projection point M as follows:

$$\begin{cases} x_4 = \frac{(x_3-x_2)^2x_1+(y_3-y_2)^2x_2+(y_1-y_2)(x_3-x_2)(y_3-y_2)}{(x_2-x_3)^2+(y_2-y_3)^2} \\ y_4 = \frac{(y_3-y_2)^2y_1+(x_3-x_2)^2y_2+(x_1-x_2)(x_3-x_2)(y_3-y_2)}{(x_2-x_3)^2+(y_2-y_3)^2} \end{cases} \tag{1}$$

2. Define the intermediate variable S, representing the distance from the point M to the point E, and calculated as follows:

$$S = 2 \cdot R \cdot \arcsin\left(\sqrt{\sin^2\left(\frac{(y_3-y_4)\pi}{360}\right) + \cos\left(\frac{y_3 \cdot \pi}{180}\right)\cos\left(\frac{y_4 \cdot \pi}{180}\right)\sin^2\left(\frac{(x_3-x_4)\pi}{360}\right)}\right)$$

(2)

Where, $R = 6378137$m denotes the radius of the earth.

3. The latitude and longitude coordinates of the point T can calculated by substituting S into Eq.(3), as follows:

$$\begin{cases} x_5 = x_4 + \frac{L(x_3 - x_4)}{S} \\ y_5 = y_4 + \frac{L(y_3 - y_4)}{S} \end{cases} \tag{3}$$

In the above, L is 2–5 times the length of the WS-USV.

Remark 2. The distance between the virtual target point and the projection point $L = nL_{WS-USV}$, L is defined as the virtual desired distance, L_{WS-USV} is the length of the WS-USV. According to the principle of line-of-sight navigation, n=2-5 is chosen in this study [38].

3.2. Heading tracking controller

The main function of the controller is to control the WS-USV at a certain speed to follow the desired path. An improved active disturbance rejection controller is designed, as described in this section.

3.2.1. Introduction of nonlinear ADRC and ELM

ADRC is a practical control method proposed by Professor Han at the end of the 20th century [39]. It is mainly composed of a tracking differentiator (TD) to reduce the overshot by arranging a transient process in the initial control state, an ESO to estimate the total disturbance, and a nonlinear state error feedback control law (NLSEF) to compensate the total disturbance by using the estimated value of ESO.

The TD part of ADRC is described as follows:

$$\begin{cases} \dot{v}_1 = v_2 \\ \dot{v}_2 = \varphi(v_1, v_2) \end{cases} \tag{4}$$

where v_1, v_2 are the outputs, $\varphi(v_1, v_2)$ is the nonlinear function.

The ESO part of ADRC is expressed as follows:

$$\begin{cases} e = z_1 - y \\ \dot{z}_1 = z_2 - \alpha_1 e \\ \dot{z}_2 = z_3 - \alpha_2 fal(e, a_1, \delta) + bu \\ \dot{z}_3 = -\alpha_3 fal(e, a_2, \delta) \end{cases} \tag{5}$$

$$fal(e, a, \delta) = \begin{cases} e\delta^{a-1}, & |e| \le \delta \\ |e|^a sign(e), & |e| > \delta \end{cases} \tag{6}$$

where the inputs of the ESO are the regulated output y and the control input u of the plant, e is the observer error, $\alpha_1, \alpha_2, \alpha_3$ are control parameters for the output error, a_1 and a_2 denote the nonlinear divisor. δ is the ESO filtering factor. z_1, z_2, z_3 are the observed values of the state variables and the unknown total disturbances.

The nonlinear state error feedback (NLSEF) control law part of ADRC is as follows:

$$\begin{cases} e_1 = v_1 - z_1 \\ e_2 = v_2 - z_2 \\ u_0 = k_P fal(e_1, \epsilon_1, \delta_0) + k_D fal(e_2, \epsilon_2, \delta_0) \\ u = u_0 - \frac{z_3}{b_0} \end{cases} \tag{7}$$

where k_P, k_D are the gain paremeters, b_0 is the compensation factor, u_0 is the amount of control before compensation, e_1, e_2 are the state error and ϵ_1, ϵ_2 are nonlinear parameters.

ELM is a fast single-hidden-layer feed-forward NN learning algorithm [40]. Its hidden layer node parameters can be randomly selected; only the number of hidden layer neurons need to be set. A unique optimal solution is obtained. The output weight of the network is a least-squared solution obtained by a minimised quadratic loss function. The parameters of the ELM need not be iterated after the determination. It is easy to use, and the calculation speed is fast. Therefore, the impetus to combine the ELM and the ADRC in practical applications is based on these merits.

The ELM algorithm is as follows. For a training data sample $\{(x_j, t_j)|x_j \in R^d, t_j \in R^m, j = 1, 2, \cdots, N\}$, the output function expression of a single hidden layer feed-forward neural network with Q hidden layer neurons is as follows:

$$\sum_{i=1}^{Q} \beta_i G(\xi_i \cdot x_j + b_i) = t_j, j = 1, 2, \cdots, N \tag{8}$$

In the above, ξ_i and b_i are the hidden layer node parameters, β_i denotes the weight vector between the i-th hidden layer and network output, and $G(\xi_i \cdot x_j + b_i)$ represents the hidden layer node output of the j-th hidden layer for sample x.

Eq.(8) can be abbreviated as $H\beta = T$. Training this network is equivalent to finding the least squares solution of the system $H\beta = T$.

$$\hat{\beta} = (H^T H)^{-1} H^T T \tag{9}$$

$$H(\xi_1, \cdots, \xi_Q, b_1, \cdots, b_Q, x_1, \cdots, x_N) = \begin{bmatrix} G(\xi_1 \cdot x_1 + b_1) & \cdots & G(\xi_Q \cdot x_1 + b_Q) \\ \vdots & \vdots & \vdots \\ G(\xi_1 \cdot x_N + b_1) & \cdots & G(\xi_Q \cdot x_N + b_Q) \end{bmatrix}_{N \times Q} \tag{10}$$

$$\beta = \begin{bmatrix} \beta_1^T \\ \vdots \\ \beta_Q^T \end{bmatrix}_{Q \times m} \qquad T = \begin{bmatrix} t_1^T \\ \vdots \\ t_N^T \end{bmatrix}_{N \times m} \tag{11}$$

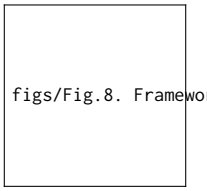

Figure 8: Framework of improved active disturbance rejection control (ADRC) for the WS-USV.

In the above, H is the output matrix of the hidden layer, and $G(\xi_i \cdot x_j + b_i)$ denotes the output of the i-th hidden layer neuron corresponding to input x_j. According to the ELM algorithm, the ELM network model for the improved active disturbance rejection controller for the WS-USV is as follows

Collect the output data $\{(Z_{1i}, Z_{2i}, Z_{3i})|Z_{1i}, Z_{2i} \in R^d, Z_{3i} \in R^m\}$ of the ESO, and use it as the training sample data;

determine the output function $G(\xi_i, b_i, Z_{1i}, Z_{2i})$ of the hidden layer, and the number of hidden layer nodes Q;

randomly generate hidden layer node parameter (ξ_i, b_i), $i = 1, 2, \cdots, Q$;

calculate the output matrix H of the hidden layer; and

calculate the output weight β of the network, as follows

$$\beta = H^+T \qquad (H^+ = (H^TH)^{-1}H^T) \tag{12}$$

The trained ELM module is embedded in the active disturbance rejection controller, and part of the output data (Z_{1i}, Z_{2i}) of the ESO is taken as the input of the ELM module. Then, the output of the ELM module is connected to a feedback loop of the control object for the ESO. The active disturbance rejection controller combined with the ELM is shown in Fig.8.

3.2.2. Design of the improved heading ADRC

The mathematical model of WS-USV is given as follows

$$\begin{cases} \dot{\psi} = r \\ \dot{r} = bP_2 + W \\ y = \psi \end{cases} \tag{13}$$

where ψ denotes the heading of WS-USV, r is the yaw velocity, P_2 is the input signal, y is the output signal, b is a position parameter, W is the total unknown dynamics.

A reference system is given as follows

$$\begin{cases} \dot{\psi}_d = r_d \\ \dot{r}_d = \varphi(\psi_d, r_d), \varphi(0,0) = 0 \end{cases} \tag{14}$$

where ψ_d is the reference input. Assume throughout this paper that $\varphi \in C(\mathrm{R}^2, \mathrm{R})$ such that the system (14) is globally asymptotically stable.

The tracking differentiator of improved ADRC is

$$\begin{cases} \dot{\psi}_{d1} = r_{d1} \\ \dot{r}_{d1} = fst(\psi_{d1}, r_{d1}, \psi_d) \end{cases} \tag{15}$$

where ψ_{d1} denotes the reference heading of WS-USV, r_{d1} is the reference yaw velocity, $fst(\psi_{d1}, r_{d1}, \psi_d)$ is the optimal synthetic rapid control function.

The improved ESO is expressed as

$$\begin{cases} e = Z_1 - \psi \\ \dot{Z}_1 = Z_2 - \beta_1 e \\ \dot{Z}_2 = Z_3 - \beta_2 fal(e, a_1, \delta_2) \\ \qquad + f_{ann}(Z_1, Z_2) + b_0 P_2 \\ \dot{Z}_3 = -\beta_3 fal(e, a_2, \delta_2) \end{cases} \tag{16}$$

where $f_{ann}(Z_1, Z_2)$ is ELM function, Z_1, Z_2 and Z_3 are the estimated values of the WS-USV state variables by the ESO, respectively. a_1, a_2, δ_2, β_1, β_2, β_3 and b_0 are adjustable parameters. e is the observation error.

The control law of the improved ADRC is

$$\begin{cases} e_1 = \psi_{d1} - Z_1 \\ e_2 = r_{d1} - Z_2 \\ u_0 = k_P fal(e_1, a, \delta_1) + k_D fal(e_2, a, \delta_1) \\ P_2 = u_0 - (Z_3 + f_{ann}(Z_1, Z_2))/b_0 \end{cases} \tag{17}$$

where a, k_P, k_D and $\delta_1$are the adjustable parameters, e_1 and e_2 are the heading error and yaw velocity error, respectively.

Assumption A1. The total unknown dynamics W of WS-USV is continuously differentiable, bounded and its first derivative is also bounded.

Assumption A2. W and the solutions ψ, r of Eq.(13), satisfy $|W|+|\psi|+|r| \le B_0$ for a constant $B_0 > 0$. $|-f_{ann}(Z_1, Z_2)|+|b - b_0||p_2| \le c^*$ for a constant $c^* > 0$.

Assumption A3. There exists constants $\bar{\omega}_{1i}(i = 1, 2, 3, 4)$, μ_{12}, μ_{13} and positive define, continuous differentiable functions V_1, Φ_1, such that

1) $\bar{\omega}_{11}\|\chi\|^2 \le V_1(\chi) \le \bar{\omega}_{12}\|\chi\|^2$, $\bar{\omega}_{13}\|\chi\|^2 \le \Phi_1(\chi) \le \bar{\omega}_{14}\|\chi\|^2$;
2) $\frac{\partial V_1(\chi)}{\partial \chi_1}(\chi_2 - g_1(\chi_1)) + \frac{\partial V_1(\chi)}{\partial \chi_2}(\chi_3 - g_2(\chi_1)) + \frac{\partial V_1(\chi)}{\partial \chi_3} g_3(\chi_1) \le -\Phi_1(\chi)$;
3) $|\frac{\partial V_1(\chi)}{\partial \chi_2}| \le \mu_{12}\|\chi\|, |\frac{\partial V_1(\chi)}{\partial \chi_3}| \le \mu_{13}\|\chi\|$.

where $\chi = (\chi_1, \chi_2, \chi_3)$, $\|\cdot\|$ denotes the Euclid norm.

Lemma 1[41]. Suppose that Assumption A1-A3 are satisfied. Then the ESO (16) is convergent.

Proof: See Appendix A.

Assumption A4. $\varphi(v)$ is continuously differentiable, $\varphi(0) = 0$, and Lipschitz continuous with Lipschitz constant L_1 : $|\varphi(v) - \varphi(\hat{v})| \leq L_1\|v - \hat{v}\|$ for all $v, \hat{v} \in \mathrm{R}^2$. There exists constants $\bar{\omega}_{2i}(i = 1, 2, 3, 4)$, μ_{22} and positive define, continuous differentiable functions V_2, Φ_2, such that

1) $\bar{\omega}_{21}\|v\|^2 \leq V_2(v) \leq \bar{\omega}_{22}\|v\|^2$, $\bar{\omega}_{13}\|v\|^2 \leq \Phi_2(v) \leq \bar{\omega}_{24}\|v\|^2$;
2) $v_2\frac{\partial V_2(v)}{\partial v_1} + \varphi(v_1, v_2)\frac{\partial V_2(v)}{\partial v_2} \leq -\Phi_2(v)$;
3) $|\frac{\partial V_2(v)}{\partial v_2}| \leq \mu_{22}\|v\|, \forall v = (v_1, v_2) \in \mathrm{R}^2$.

In above assumption, the continuous differentiability and Lipschitz continuity of $\varphi(\cdot)$ imply that

$$|\frac{\partial \varphi(v)}{\partial v_i}| \leq L_1, v \in \mathrm{R}^2, i = 1, 2. \tag{18}$$

Assumption A5. Both ψ_d and $\dot{\psi}_d = r_d$ are bounded in $[0, \infty)$, and $\varphi(\cdot)$ is locally Lipschitz continuous, and system (15) with $\psi_d \equiv 0$ is globally asymptotically stable.

The proof of Assumption A5 is given in the Theorem 3.1 of Ref.[42].

Lemma 2[43]. Suppose that Assumption A1-A5 are satisfied. Then the tracking errors $\psi_{d1} - \psi$ and $r_{d1} - r$ are convergent.

Proof: See Appendix B.

To convert the mathematical form of the controller into C code and integrate it into the control system of a WS-UVS, the improved active disturbance rejection controller must be discretised. The TD discrete algorithm is expressed as follows:

$$\begin{cases} \psi_{d1}(k+1) = \psi_{d1}(k) + Tr_{d1}(k) \\ r_{d1}(k+1) = r_{d1}(k) + Tfst(\psi_{d1}(k), r_{d1}(k), \\ \qquad\qquad \psi_d(k), r, h) \end{cases} \tag{19}$$

where T denotes the sampling period of the control system, $fst(\psi_{d1}, r_{d1}, \psi_d, r, h)$ is the optimal synthetic rapid control function, ψ_d denotes the direction angle between the current position and desired position of the WS-USV, and is the input signal of the path-following system, ψ_{d1} and r_{d1} are the states of the tracking system, and r and h are adjustable parameters used to adjust the frequency and filtering effect of the tracking differentiator.

For the second-order system, the ESO discrete algorithm can be described as follows

$$\begin{cases} e(k) = Z_1(k) - \psi(k) \\ Z_1(k+1) = Z_1(k) + T(Z_2(k) - \beta_1 e(k)) \\ Z_2(k+1) = Z_2(k) + T(Z_3(k) \\ -\beta_2 fal(e(k), a_1, \delta_2) + f_{ann}(Z_1, Z_2) + b_0 P_2(k)) \\ Z_3(k+1) = Z_3(k) - T\beta_3 fal(e(k), a_2, \delta_2) \end{cases} \tag{20}$$

where $f_{ann}(Z_1, Z_2)$ is ELM function, which is described as follows

$$f_{ann}(Z_1, Z_2) = \sum_{i=1}^{Q} \zeta_i(\frac{1}{1+e^{-(\xi_{1i}Z_1+b_i)}} + \frac{1}{1+e^{-(\xi_{2i}Z_2+b_i)}}) \tag{21}$$

The discrete algorithm of the NLSEF control law is described as follows

$$\begin{cases} e_1(k) = \psi_{d1}(k) - Z_1(k) \\ e_2(k) = r_{d1}(k) - Z_2(k) \\ u_0(k) = k_P fal(e_1(k), a_1, \delta_1) \\ +k_D fal(e_2(k), a_2, \delta_1) \\ P_2(k) = u_0 - (Z_3(k) + f_{ann}(Z_1, Z_2))/b_0 \end{cases} \tag{22}$$

In the above, $Z_1(k)$, $Z_2(k)$ and $Z_3(k)$ are the estimation values of the ship state variables by the ESO. $\psi(k)$ is the controlled output of the system, δ_2, β_1, β_2 and β_3 are adjustable parameters. k_P, k_D, δ_1, a_1 and a_2 are the adjustable parameters. $P_2(k)$ is the output value of the controller, and can be input into the propeller controller after the corresponding transformation.

$$P_c(k) = P_1(k) + P_2(k)\begin{bmatrix} -1 \\ 1 \end{bmatrix} \tag{23}$$

where $P_c(k) = [P_{c1}(k), P_{c2}(k)]^T$ is the converted output value vector, and $P_1(k) = [P_{1l}(k), P_{1r}(k)]^T$ is the vector consisting of the duty cycles corresponding to the desired speeds of the left and right propellers.

The WS-USV adopts a twin-propeller propulsion mode without a rudder module, and only steers through the speed difference of the twin-propeller. The relationship between the propeller speed difference and yaw moment is espressed as follows [44]

$$N_P = k(n_l - n_r)d_P \tag{24}$$

In the above, k is the conversion coefficient, N_P is the yaw moment, n_l and n_r are the rotation speeds of the left and right propellers, respectively, and d_P is the installation distance of the left and right propellers.

Owing to the structural characteristics of the propeller, it is governed by multiple input constraints. The inherent control law of the propeller is shown in Table.1, the speeds

Table 1
Control law of the propeller

positive pulse width range (period 8ms)	propeller status
1.5ms	stop
1.5ms–2.2ms	forward rotation, speed increase
1.5ms–0.8ms	reverse rotation, speed increase

for forward and reverse rotation of the propeller are limited. The frequent operation of the propeller at an extreme speed will significantly increase the wear, affecting the stability of the system.

The duty cycles corresponding to the pulse width range are 1.5ms for 150, 1.5ms–2.2ms for 150–220, and 1.5ms–0.8 ms for 150–80, respectively.

As the WS-USV is steered based on twin-propeller rotation speed difference, in the course of an attitude adjustment, the propeller will frequently switch between forward and reverse rotation. Even when the steering demand is large, switches from the forward maximum speed to reverse maximum speed often occur. However, this cannot be achieved in a short period of time, and has a great impact on the propellers and hardware system of the WS-USV, as well as the stability of the entire control system [45]. According to Eq.(13), the greater the rotation speed difference of the twin-propeller, the greater the yaw moment. If the steering is too fast, the tracking effect will be poor, and the tracking performance will be unstable. Considering the above engineering practice, in the design process of the controller, a saturation function is introduced to limit the amplitude and speed of the control input to reduce the adverse effects and enhance the stability of the system.

When the WS-USV is sailing forward, the calculation is as follows

$$P_{ii}(k)=\begin{cases}200 & \text{if} \quad P_{ci}(k)\geq 200(i=1,2)\\ P_{ci}(k) & \text{if} \quad 150<P_{ci}(k)<200\\ 150 & \text{if} \quad P_{ci}(k)\leq 150\end{cases} \tag{25}$$

When the WS-USV is sailing backward, the calculation is as follows

$$P_{ii}(k)=\begin{cases}100 & \text{if} \quad P_{ci}(k)\leq 100(i=1,2)\\ P_{ci}(k) & \text{if} \quad 100<P_{ci}(k)<150\\ 150 & \text{if} \quad P_{ci}(k)\geq 150\end{cases} \tag{26}$$

In the above, $P(k)=[P_{11}(k),P_{22}(k)]^T$ denotes the vector consisting of the control output after conversion and engineering restrictions.

Remark 3. Compared with robust control methods that are based on the worst case design, the robustness of ADRC may not be as good as these methods since they are designed to achieve best possible robust performance in the presence of the worst uncertainty. Thus, ADRC can be regarded as a "refined" robust control method. However, it provides a promising approach for trading off between the nominal performance and robustness. Above all, ADRC provides an alternative approach to widely used robust control and adaptive control methods for dealing with uncertain systems.

Remark 4. It is demonstrated in [46] that nonlinear ESO has better tracking performance in low frequency bands than linear ESO, but worse tracking performance in high frequency bands than linear ESO. For ship motion control, the low frequency position information of the ship and the low frequency disturbance that can cause ship position change. The high frequency signals caused by ocean disturbances need to be filtered out. From this point of view, nonlinear ESO is more suitable for the needs of state and disturbance estimation in ship motion control. Furthermore, the propeller suffers from the constraint of thrust amplitude due to the inherent characteristics. In order to alleviate the effect of amplitude limitation and improve the stability of the system, the nonlinear saturation function is introduced for the controller design. It is clear that the WS-USV is a complex nonlinear system with strong uncertainty. From this point of view, ADRC is more suitable for the controller design than LADRC.

Remark 5. It is shown in [47] that a NN-based ADRC has better dynamic characteristics than ADRC. In order to clarify the reason of using the ELM, we compare it with back propagation neural network (BPNN). Compared with the training speed and structure, we find that the ELM is fast in training speed and simple in structure. In the ELM training process, there is no need to adjust the number of hidden layer neurons and the only optimal solution can be obtained. The training of ELM is simplified since ELM works for generalized single-hidden layer feed-forward networks. However, BPNN has multi-layer hidden layer and the training process is complex. ELM has faster learning speed and better generalization performance. In addition, ELM is easier to be implemented in the ARM control module than BPNN.

Remark 6. The main work of this paper is the application of improved nonlinear ADRC to the heading control of WS-USV based on the milestone theoretical analysis of the convergence of nonlinear ADRC in [41, 42, 43]. The effectiveness and stability of the designed nonlinear heading ADRC are proved from the perspective of practice by a large number of navigation experiments of WS-USV. A brief theoretical analysis of nonlinear heading ADRC is given in Appendix A and B. For a detailed analysis of the convergence of nonlinear ADRC, authors can refer to Ref.[41, 42, 43].

4. Experimental and result analysis of water sampling

4.1. Setting of water sampling target points

The WS-USV prototype is shown in Fig.9.

Before water sampling starts, the target sampling points must be selected according to the requirements of the water sample collection. According to the principle of random

Figure 9: WS-USV prototype.

sampling, five target points were selected, i.e. the middle and four corners of the water sampling area. The latitude and longitude coordinates of the five sampling points were measured by GPS, and were sent to the WS-USV by the remote control platform. The latitude and longitude coordinates of the five desired sampling points used in this experiment are shown in Table 2.

Table 2
Coordinates of water sampling points.

Sampling point number	Longitude	Latitude
1	118.083457° E	24.581749° N
2	118.083950° E	24.581277° N
3	118.083940° E	24.582722° N
4	118.082936° E	24.582699° N
5	118.083116° E	24.581123° N

4.2. Testing of automatic water sampling navigation

In this experiment, a single closed-loop control method for heading based on a constant speed was adopted to test the automatic path-following control performance, perform a real-time comparison of the current heading and desired heading in the navigation process, provide real-time recording of heading errors, and change the left and right propellers' rotation speeds to adjust the course. The traditional ADRC method path-following control performance test and improved ADRC strategy path-following control performance test were conducted in this experiment. This experiment was conducted in a sea area with a grade 4 westerly wind, and it was cloudy. In the process of the experiment, the distance threshold, yaw angle threshold, and reference speed of the WS-USV were set as 3m, 3° and 1.2m/s, respectively. The threshold meant that when the difference between the current value and desired value was less than the threshold value, the current value could be regarded as equal to the desired value. The velocity factor r_0 , sampling step h_0, sampling time t and parameter δ of the ADRC took empirical values of 3000, 0.005, 0.01 and 0.1, respectively. After many experiments, the diagram of the water sampling path and contrast curve between the actual heading and desired heading of the WS-USV path-following controller was designed based on the ADRC technology. Its depiction in the HMI is shown in Fig.10. The control parameters b_0, β_1, β_2, β_3, k_P and k_D were 1.3, 85.5, 2436.75, 23149.5, 2.95 and 0.55, respectively.

a. Diagram of the water sampling path.

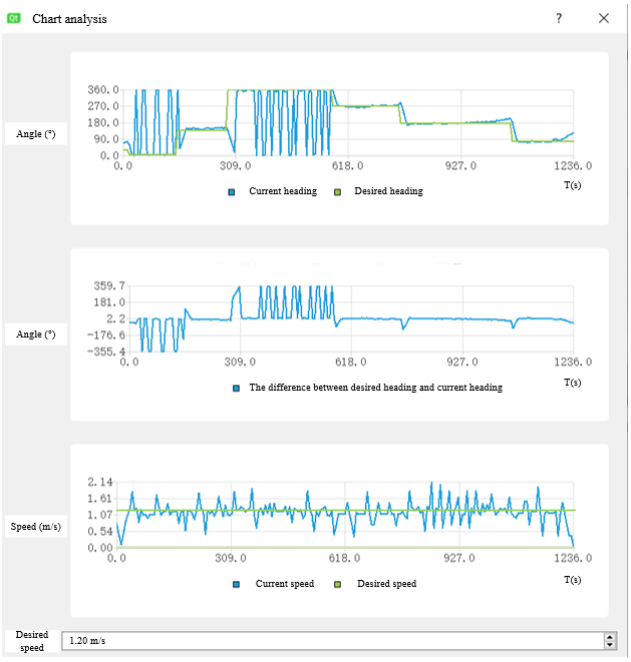

b. Diagram of course and speed tracking.

Figure 10: Diagram of water sampling path tracking control for the ADRC.

The same control parameters were adopted in the WS-USV path-following controller based on the ADRC method combined with ELM. The offsets a and b of the hidden layer and output layer of the ELM were 0.46 and 0.367, respectively, and the learning rate was set as 0.352. The corresponding input weights are listed in Table.3.

After ELM training, the diagram of the water sampling path and contrast curve between the actual heading and desired heading of the WS-USV path-following controller based on the ADRC strategy combined with ELM were depicted in the HMI, as shown in Fig.11.

Specification of speed and course tracking diagram: As the range of the heading collected by electronic compass

Table 3
Input weights of each neuron

Neuron number	Input weight
1	(-0.04824, 0.03983)
2	(-0.26338, -0.89235)
3	(0.31122, 0.72437)
4	(0.87640, -0.11413)
5	(0.24085, 0.09602)
6	(-0.43432, 0.13372)
7	(-0.58964, 0.36079)
8	(-0.12173, -0.25724)
9	(-0.94550, -0.84354)
10	(0.75237, -0.08730)
11	(0.22018, -0.90431)
12	(-0.59282, 0.47651)

was 0° to 360° and the desired heading corresponding to the second tracking point was 359.74°, there was a leap from 360° to 0° within the normal range. Thus, the difference between the actual heading and desired heading as shown in the course tracking diagram did not exceed the angle threshold range, and the course tracking was normal. Comparisons of the water sampling paths based on the traditional ADRC method and improved ADRC strategy are shown in Fig.12.

The actual headings of the WS-USV based on the traditional ADRC method and improved ADRC strategy are depicted in Fig.13. It can be seen from Fig.10-Fig.13 that the two path-following controllers (the traditional ADRC technology and the improved ADRC method) had the same desired speed in the process of multiple-point water sampling. The error between the improved ADRC water sampling path and desired path is less than the difference from the traditional ADRC method. The improved ADRC strategy yaw angle jump is smaller and more stable, where as the traditional ADRC method yaw angle oscillation is relatively large. In summary, the control system designed based on the two control methods is effective and stable, and the control performance of the improved ADRC method is slightly superior to that of the traditional ADRC technology.

The real-time duty cycles of the left and right propellers are processed by amplitude limiting and speed limiting. For example, the duty ratios correspond to the real-time speeds of the left and right propellers, as shown in Fig.14.

The duty cycle difference corresponding to the real-time rotation speed difference between the left and right propellers is shown in Fig.15. It can be seen from Fig.14 and Fig.15 that the rotation speed and rotation speed difference for the left and right propellers are kept within a limited range, and the rotation speed is kept within the maximum speed range of 0 to 71.5%. This significantly reduces the abnormal wear caused by frequent use of maximum speed, and also prevents instability in the system and running errors in the control program caused by the sudden switching from forward to reverse in the propeller. The rotation speed difference of the propellers is maintained within a proper range, which reduces the amplitude and frequency of the yaw of the WS-

a. Diagram of the water sampling path.

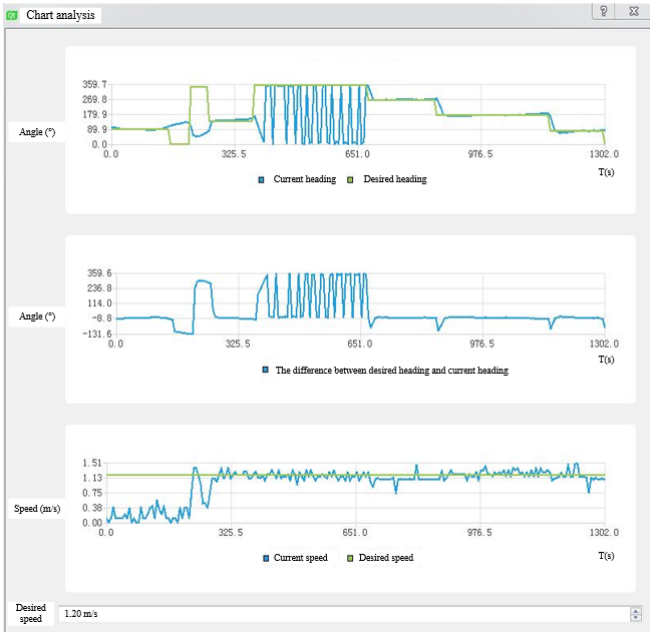

b. Diagram of course and speed tracking.

Figure 11: Diagram of water sampling path tracking control for the improved ADRC.

USV and is conducive to a stable sail. However, the performance of the WS-USV in emergency obstacle avoidance or large winds and waves will be affected by the relevant restrictive treatment. In view of this situation, a gear shift function is added to the design of the WS-USV system. All restrictions are removed by automatically shifting gears, and the maximum speed and maximum yaw moment are restored to cope with the emergency.

5. Conclusion

In this study, a set of WS-USV systems is designed, including a remote automatic control platform, joystick remote controller, and USV. An automatic path-following control system based on an ARM controller combined with GPS and an electronic compass is developed for a WS-USV. Aiming at practical engineering problems (such as frequent switching bewteen extreme speed causes system instability), an improved ADRC strategy is proposed. A saturation function is

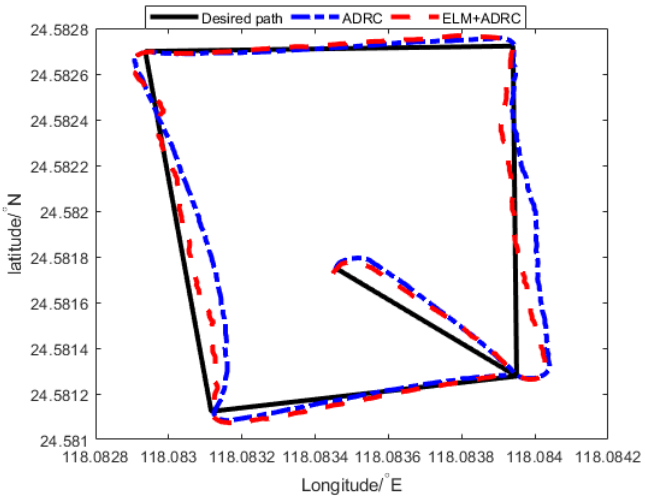

Figure 12: Water sampling paths.

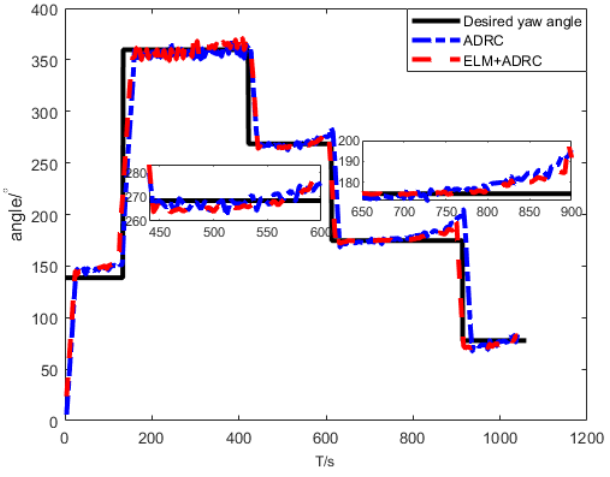

Figure 13: Desired and actual yaw angles of the WS-USV.

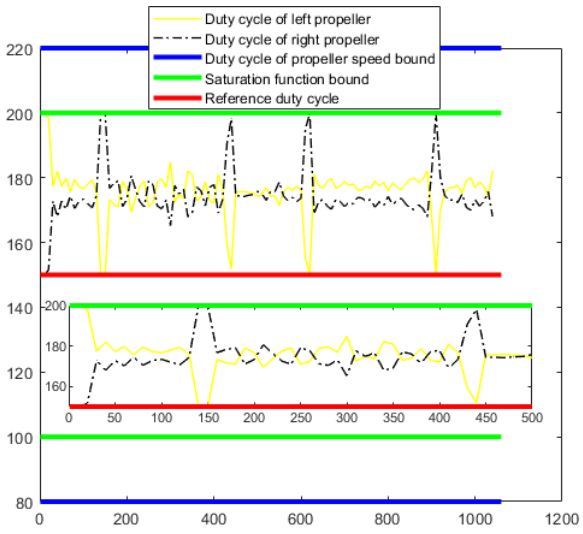

Figure 14: Duty cycles of the left and right propellers.

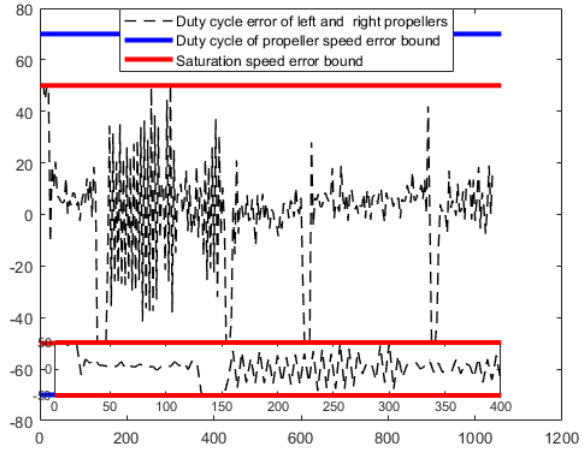

Figure 15: Duty cycle errors of the left and right propellers.

introduced into the controller design to address limitations regarding amplitude and rate, ensuring the stability of the control system and reducing the wear of the propeller. A constant speed and heading closed-loop control is adopted for the design of the WS-USV control system. The WS-USV comprises multi-point automatic sampling equipment with a remote controller that integrates manual remote control, key control, and important parameter displays, and a convenient remote automatic control platform providing functions for map display, manual control, video recording, parameter display, and water sampling. The feasibility and stability of the control system are verified by multi-group water sampling experiments. The comparisons of the traditional ADRC and improved ADRC indicate that the control effect of the improved ADRC is better than that of the traditional ADRC.

Acknowledgements

The authors are grateful for the comments raised by the reviewers which helped significantly improve the quality of the paper. The authors would like to express appreciation for the financial support provided by the National Natural Science Foundation of China (51809113, 52171309), Fujian Provincial Science and Technology Department (2019H0019) and Fujian Provincial Young Top-Notch Talent Plan(Z02101).

Appendix A

Proof of Lemma 1.

Proof. With an extended state variable $x_3 = W + (b - b_0)P_2$,

the system (13) can be written as:

$$\begin{cases} \dot{x_1} = \dot{\psi} = r \\ \dot{x_2} = \dot{r} = bP_2 + W \\ \dot{x_3} = \dot{W} + (b - b_0)\dot{P}_2 = h \\ y = x_1 = \psi \end{cases} \tag{27}$$

where $h = \dot{W} + (b - b_0)\dot{P}_2$.

From Assumption A1 and A2, there is a positive constant $h^* > 0$ such that $|\dot{W} + (b - b_0)\dot{P}_2| = |h| < h^*$ for all $t \geq 0$. Set

$$\begin{cases} E_1 = \psi - Z_1 \\ E_2 = r - Z_2 \\ E_3 = (W + (b - b_0)P_2) - Z_3 \\ g_1(E_1) = -\beta_1 E_1 \\ g_2(E_1) = -\beta_2 fal(E_1, a_1, \delta_2) \\ g_3(E_1) = -\beta_3 fal(E_1, a_2, \delta_2) \end{cases} \tag{28}$$

According to (24),(26) and (27), we have $E = [E_1, E_2, E_3]^T$ satisfies

$$\begin{cases} \dot{E}_1 = E_2 - g_1(E_1) \\ \dot{E}_2 = E_3 - g_2(E_1) - f_{ann}(Z_1, Z_2) + (b - b_0)P_2 \\ \dot{E}_3 = h - g_3(E_1) \end{cases} \tag{29}$$

By Assumption A3, finding the derivative of $V_1(E) = \frac{1}{2}E_1^2 + \frac{1}{2}E_2^2 + \frac{1}{2}E_3^2$ with respect to t along the solution E of Eq.(29).

$$\begin{aligned} \frac{\mathrm{d}}{\mathrm{d}t}V_1(E) &= \frac{\partial V_1(E)}{\partial E_1}(E_2 - g_1(E_1)) + \frac{\partial V_1(E)}{\partial E_2}(E_3 \\ &\quad - g_2(E_1)) - \frac{\partial V_1(E)}{\partial E_3}g_3(E_1) \\ &\quad + \frac{\partial V_1(E)}{\partial E_2}(-f_{ann}(Z_1, Z_2) \\ &\quad + (b - b_0)P_2) + \frac{\partial V_1(E)}{\partial E_3}h \\ &\leq -\Phi_1(E) + c^*\mu_{12}\|E\| + h^*\mu_{13}\|E\| \\ &\leq -\frac{\bar{\omega}_{13}}{\bar{\omega}_{12}}V_1(E) + \frac{\sqrt{\bar{\omega}_{11}}}{\bar{\omega}_{11}}(c^*\mu_{12} \\ &\quad + h^*\mu_{13})\sqrt{V_1(E)} \end{aligned} \tag{30}$$

It follows that

$$\frac{\mathrm{d}}{\mathrm{d}t}\sqrt{V_1(E)} \leq -\frac{\bar{\omega}_{13}}{2\bar{\omega}_{12}}\sqrt{V_1(E)} + \frac{\sqrt{\bar{\omega}_{11}}}{2\bar{\omega}_{11}}(c^*\mu_{12} + h^*\mu_{13}) \tag{31}$$

By Assumption A3 again, we have

$$\begin{aligned} \|E\| \leq \sqrt{\frac{V_1(E)}{\bar{\omega}_{11}}} &\leq \frac{\sqrt{\bar{\omega}_{11}V_1(E(t_1))}}{\bar{\omega}_{11}}\mathrm{e}^{-\frac{\bar{\omega}_{13}}{2\bar{\omega}_{12}}(t-t_1)} \\ &\quad + \frac{c^*\mu_{12} + h^*\mu_{13}}{2\bar{\omega}_{11}}\int_{t_1}^{t}\mathrm{e}^{-\frac{\bar{\omega}_{13}}{2\bar{\omega}_{12}}(t-s)}\mathrm{d}s \leq B_* \end{aligned} \tag{32}$$

This together with (27) yields

$$\begin{aligned} |E_j| \leq \|E\| &\leq \frac{\sqrt{\bar{\omega}_{11}V_1(E(t_1))}}{\bar{\omega}_{11}}\mathrm{e}^{-\frac{\bar{\omega}_{13}}{2\bar{\omega}_{12}}(t-t_1)} \\ &\quad + \frac{c^*\mu_{12} + h^*\mu_{13}}{2\bar{\omega}_{11}}\int_{t_1}^{t}\mathrm{e}^{-\frac{\bar{\omega}_{13}}{2\bar{\omega}_{12}}(t-s)}\mathrm{d}s \\ &\quad \overset{t\to\infty}{\longrightarrow} 0, (j = 1, 2, 3) \end{aligned} \tag{33}$$

Therefore, the ESO is convergent. The proof is complete.

Appendix B

Proof of Lemma 2.

Proof. Set

$$\eta = [\eta_1, \eta_2]^T, \eta_1 = \psi_{d1} - \psi, \eta_2 = r_{d1} - r. \tag{34}$$

From (15),(17),(27) and (34), it follows that

$$\begin{cases} \dot{\eta}_1 &= \eta_2 \\ \dot{\eta}_2 &= -\varphi(\eta_1, \eta_2) - E_3 - [\varphi(e_1, e_2) \\ &\quad -\varphi(\psi_{d1} - \psi, r_{d1} - r)] \end{cases} \tag{35}$$

By Lipschitz continuity of $\varphi(\cdot)$ assumed in Assumption A4, we have

$$\begin{aligned} &|\varphi(\psi_{d1} - Z_1, r_{d1} - Z_2) - \varphi(\psi_{d1} - \psi, r_{d1} - r)| \\ &\quad \leq L_1\|[\psi - Z_1, r - Z_2]^T\| \leq L_1\|[E_1, E_2]^T\| \end{aligned} \tag{36}$$

Under Assumption A4 and using (36), we can compute the derivative of $V_2(\eta) = \frac{1}{2}\eta_1^2 + \frac{1}{2}\eta_2^2 = \frac{1}{2}(\psi_{d1} - \psi)^2 + \frac{1}{2}(r_{d1} - r)^2$ along the solution of (35) as follows:

$$\begin{aligned} \frac{\mathrm{d}V_2(\eta)}{\mathrm{d}t} &= \eta_2\frac{\partial V_2(\eta)}{\partial \eta_1} - \{\varphi(\eta) + E_3 + [\varphi(e_1, e_2) \\ &\quad - \varphi(\psi_{d1} - \psi, r_{d1} - r)]\}\frac{\partial V_2(\eta)}{\partial \eta_2} \\ &\leq -\Phi_2(\eta) + (L + 1)\mu_{22}\|E\|\|\eta\| \\ &\leq -\frac{\bar{\omega}_{23}}{\bar{\omega}_{22}}V_2(\eta) + N_*\sqrt{V_2(\eta)}, \forall t > t_2 \end{aligned} \tag{37}$$

where N_* is some R-dependent positive constant and we used the face $\|E\| \leq B_*$ proved in (31). It then follows that

$$\frac{\mathrm{d}\sqrt{V_2(\eta)}}{\mathrm{d}t} \leq -\frac{\bar{\omega}_{23}}{\bar{\omega}_{22}} V_2(\eta) + N_*, \forall t > t_2 \tag{38}$$

This together with Assumption A4 implies that for all $t > t_2$, that

$$\begin{aligned} \|\eta\| \leq \sqrt{\frac{V_2(\eta)}{\bar{\omega}_{21}}} \leq \frac{\sqrt{\bar{\omega}_{21}}}{\bar{\omega}_{21}} (\mathrm{e}^{-\frac{\bar{\omega}_{23}}{\bar{\omega}_{22}}(t-t_2)} \sqrt{V_2(\eta(t_2))} \\ + N_* \int_{t_2}^{t} \mathrm{e}^{-\frac{\bar{\omega}_{23}}{\bar{\omega}_{22}}(t-s)} \mathrm{d}s) \end{aligned} \tag{39}$$

Since the first term of the right-hand side of (39) tends to zero as t goes to infinity, and the second term is bounded, it follows that there exist $t_1 > t_2$ and $\Gamma_2 > 0$ such that $\|[\psi_{d1} - \psi, r_{d1} - r]^T\| \leq \Gamma_2$ for all $t > t_1$. Thus the tracking errors $\psi_{d1} - \psi$ and $r_{d1} - r$ are convergent. The proof is complete.

References

[1] Dongming Xie, Qinghua Huang, Shi Xu, Yangming Zhou, Guohong Zhou, Junsong Jia, and Zaiyu Zhu. Assessment of surface water quality in lushan: A world heritage sites in china. *Environmental Science and Pollution Research*, 17:18934–18948, 2020.

[2] Chamara Pliyanage, Ashu Marasinghe, and Koichi Yamada. Comparison of optimized selection methods of sampling sites network for water quality monitoring in a river. *International Journal of Affective Engineering*, 15(2):195–204, 2016.

[3] Zhouhua Peng, Jun Wang, and Dan Wang. Distributed containment maneuvering of multiple marine vessels via neurodynamics-based output feedback. *IEEE Transactions on Industrial Informatics*, 64(5):3831–3839, 2017.

[4] Tingting Yang, Yuejun Guo, Yi Zhou, and Siwen Wei. Joint communication and control for small underactuated USV based on mobile computing technology. *IEEE Access*, 7:160610–160622, 2019.

[5] Zhixiang Liu, Youmin Zhang, Xiang Yu, and Chi Yuan. Unmanned surface vehicles: An overview of developments and challenges. *Annual Reviews in Control*, 41:71–93, 2016.

[6] Zaopeng Dong, Tao Bao, Mao Zheng, Xin Yang, Lifei Song, and Yunsheng Mao. Heading control of unmanned marine vehicles based on an improved robust adaptive fuzzy neural network control algorithm. *IEEE Access*, 7:9704–9713, 2019.

[7] Yunsheng Fan, Xiaojie Sun, Guofeng Wang, and Chen Guo. On fuzzy self-adaptive PID control for USV course. In *Proceedings of the 34th Chinese Control Conference*, pages 8472–8478, Hangzhou, China, 2015.

[8] M. H. Moradi and M. R. Katebi. Predictive PID control for ship autopilot design. *IFAC Proceedings Volumes*, 34(7):375–380, 2001.

[9] Ming-Chung Fang, Young-Zoung Zhuo, and Zi-Yi Lee. The application of the self-tuning neural network pid controller on the ship roll reduction in random waves. *Ocean Engineering*, 37:529–538, 2010.

[10] Anthony J. Healey and David Lienard. Multivariable sliding-mode control for autonomous diving and steering of unmanned underwater vehicles. *IEEE Journal of Oceanic Engineering*, 18(3):327–339, 1993.

[11] Li-Ying Hao, He Zhang, Wei Yue, and Hui Li. Fault-tolerant compensation control based on sliding mode technique of unmanned marine vehicles subject to unknown persistent ocean disturbances. *International Journal of Control, Automation and Systems*, 18(3):739–752, 2020.

[12] Chaodong Hu, Defeng Wu, Yuxiang Liao, and Xin Hu. Sliding mode control unified with the uncertainty and disturbance estimator for dynamically positioned vessels subjected to uncertainties and unknown disturbances. *Applied Ocean Research*, 109:102564, 2021.

[13] Yingjie Deng, Xianku Zhang, Namkyun Im, Guoqing Zhang, and Qiang Zhang. Adaptive fuzzy tracking control for underactuated surface vessels with unmodeled dynamics and input saturation. *ISA Transactions*, 103:52–62, 2020.

[14] Zhouhua Peng, Jun Wang, and Dan Wang. Distributed maneuvering of autonomous surface vehicles based on neurodynamic optimization and fuzzy approximation. *IEEE Transactions on Control Systems Technology*, 26(3):1083–1090, 2018.

[15] Defeng Wu, Yuxiang Liao, Chaodong Hu, Shuanghe Yu, and Qingyuan Tian. An enhanced fuzzy control strategy for low-level thrusters in marine dynamic positioning systems based on chaotic random distribution harmony search. *International Journal of Fuzzy Systems*, DOI:10.1007/s40815-020-00989-5, 2020.

[16] Chang Wang, Hairong Xiao, and Yaozhen Han. Applications of adrc in unmanned surface vessel course tracking. *Applied Mechanics and Materials*, 427-429:897–900, 2013.

[17] Youqiang Huang, Defeng Wu, Zibin Yin, and Zhi-Ming Yuan. Design of UDE-based dynamic surface control for dynamic positioning of vessels with complex disturbances and input constraints. *Ocean Engineering*, 220:108487, 2021.

[18] Cheng Liu, C. L. Philip Chen, Zaojian Zou, and Tieshan Li. Adaptive NN-DSC control design for path following of underactuated surface vessels with input saturation. *Neurocomputing*, 276:466–474, 2017.

[19] Bong Seok Park, Ji-Wook Kwon, and Hongkeun Kim. Neural network-based output feedback control for reference tracking of underactuated surface vessels. *Automatica*, 77:353–359, 2017.

[20] Zhouhua Peng, Jun Wang, and Qing-Long Han. Path-following control of autonomous underwater vehicles subject to velocity and input constraints via neurodynamic optimization. *IEEE Transactions on Industrial Electronics*, 66(11):8724–8732, 2019.

[21] Hongde Qin, Chengpeng Li, and Yanchao Sun. Adaptive neural network-based fault-tolerant trajectory-tracking control of unmanned surface vessels with input saturation and error constraints. *IET Intelligent Transport Systems*, 14(5):3624–3638, 2020.

[22] Yongpeng Weng and Ning Wang. Data-driven robust backstepping control of unmanned surface vehicles. *International Journal of Robust Nonlinear Control*, 30(9):3624–3638, 2020.

[23] Pengfei Zhang and Ge Guo. Fixed-time switching control of underactuated surface vessels with dead-zones: Global exponential stabilization. *Journal of the Franklin Institute*, 357(16):11217–11241, 2020.

[24] Tieshan Li, Rong Zhao, C. L. Philip Chen, Liyou Fang, and Cheng liu. Finite-time formation control of underactuated ships using nonlinear sliding mode control. *IEEE Transactions on Cybernetics*, 48(11):3243–3253, 2018.

[25] Chengju Zhang, Cong Wang, Yingjie Wei, and Jinqiang Wang. Neural network adaptive position tracking control of underactuated autonomous surface vehicle. *Journal of Mechanical Science and Technology*, 2(34):855–865, 2020.

[26] Zewei Zheng, Linping Ruan, Ming Zhu, and Xiao Guo. Reinforcement learning control for underactuated surface vessel with output error constraints and uncertainties. *Neurocomputing*, 399:479–490, 2020.

[27] Walyer Caharija, Kristin Y. Pettersen, Marco Bibuli, Pedro Calado, Enrica Zereik, José Braga, Jan Tommy Gravdahl, Asgeir J. Sørensen, Milan Milovanović, and Gabriele Bruzzone. Integral line-of-sight guidance and control of underactuated marine vehicles: Theory, simulations, and experiments. *IEEE Transactions on Control Systems Technology*, 24(5):1623–1642, 2016.

[28] Lepeng Chen, Rongxin Cui, Chengguang Yang, and Weisheng Yan. Adaptive neural network control of underactuated surface vessels with guaranteed transient performance: Theory and experimental results. *IEEE Transactions on Industrial Electronics*, 67(5):4024–4035, 2020.

[29] Chengzhi Ruan, Dean Zhao, Yueping Sun, Jianqing Hong, Shihong Ding, and Ji Luo. Design and testing of a control system associated

with the automatic feeding boat for farming chinese river crabs. *Computers and Electronics in Agriculture*, 150:14–25, 2018.

[30] Yue Jiang, Zhouhua Peng, Dan Wang, and C. L. Philip Chen. Line-of-sight target enclosing of an underactuated autonomous surface vehicle with experiment results. *IEEE Transactions on Industrial Informatics*, 16(2):832–841, 2020.

[31] Ning Wang and Xinxiang Pan. Path following of autonomous underactuated ships: A translation-rotation cascade control approach. *IEEE/ASME Transactions on Mechatronics*, 24(6):2583–2593, 2019.

[32] Bikram Pratap Banerjee, Simit Raval, Thomas J Maslin, and Wendy Timms. Development of a UAV-mounted system for remotely collecting mine water samples. *International Journal of Mining, Reclamation and Environment*, 34(6):385–396, 2020.

[33] Cengiz Koparan, Ali Bulent Koc, Charles V. Privette, Calvin B. Sawyer, and Sharp Julia L. Evaluation of a UAV-assisted autonomous water sampling. *Water*, 10(5):1–16, 2018.

[34] Defeng Wu, Zi Ma, Aiguo Li, and Quanmin Zhu. Identification for fractional order rational models based on particle swarm optimization. *International Journal of Computer Applications in Technology*, 41(1-2):53–59, 2011.

[35] Syuan-Yi Chen, Cheng-Yen Lee, Chien-Hsun Wu, and Yi-Hsuan Hung. Intelligent motion control of voice coil motor using pid-based fuzzy neural network with optimized membership function. *Engineering Computations*, 33(8):2302–2319, 2016.

[36] Yonghui Xie, Xujie Hou, and Xiaoyan Yang. Design of embedded HMI universal platform and its application in mounter. *2020 3rd International Conference on Advanced Electronic Materials, Computers and Software Engineering*, pages 909–913, 2020.

[37] Tobias Holstein, Bastian Weiβbach, and Joachim Wietzke. Towards a HTML-UI-Compositor by introducing the wayland-protocol into a browser-engine. pages 192–200, 2016.

[38] Peng Han, Zhilin Liu, Zecai Zhou, hao Tang, Liang Ban, and Liulei Hao. Path tracking control algorithm based on LOS method for surface self-propulsion vessel. *Applied Science and Technology*, 45(3):66–70, 2018(In Chinese).

[39] Jingqing Han. From PID to active disturbance rejection control. *IEEE Transactions on Industrial Electronics*, 56(3):900–906, 2009.

[40] Guang-Bin Huang. An insight into extreme learning machines: Random neurons, random features and kernels. *Cognitive Computation*, 6:376–390, 2014.

[41] Baozhu Guo and Zhiliang Zhao. On the convergence of an extended state observer for nonlinear systems with uncertainty. *System & Control Letters*, 60(6):420–430, 2011.

[42] Baozhu Guo and Zhiliang Zhao. On convergence of tracking differentiator. *International Journal of Control*, 84(4):693–701, 2011.

[43] Zhiliang Zhao and Baozhu Guo. On convergence of nonlinear active disturbance rejection control for SISO nonlinear systems. *Journal of Dynamical and Control Systems*, 22:385–412, 2016.

[44] Anil Kumar Dash, Vishwanath Nagarajan, and Om Prakash Sha. Bifurcation analysis of a high-speed twin-propeller twin-rudder ship maneuvering model in roll-coupling motion. *Nonlinear Dynamics*, 83:2035–2053, 2016.

[45] Jun Nie and Xiaogong Lin. Robust nonlinear path following control of underactuated MSV with time-varying sideslip compensation in the presence of actuator saturation and error constraint. *IEEE Access*, 6:71906–71917, 2018.

[46] Haiqiang Wang and Hai Huang. Property and applications of extended state observer. *Control and Decision*, 28(7):1078–1082, 2013 (In Chinese).

[47] Tommaso Matassini, Hyo Sang Shin, Antonios Tsourdos, and Mario Innocenti. Adaptive control with neural networks-based disturbance observer for a spherical UAV. *IFAC-PapersOnLine*, 49(17):308–313, 2016.